

## 23

# Coherent Structures and Mixing at a River Plume Front

Alexander R. Horner-Devine,<sup>1</sup> C. Chris Chickadel,<sup>2</sup>  
& Daniel G. MacDonald<sup>3</sup>

<sup>1</sup>Civil and Environmental Engineering, University of Washington, United States

<sup>2</sup>Applied Physics Laboratory, University of Washington, United States

<sup>3</sup>Department of Estuarine and Ocean Sciences, University of Massachusetts, United States

## ABSTRACT

Despite years of research on the dynamics and mixing of gravity currents, there are relatively few detailed observations at geophysical scales. In this chapter, we present measurements of the frontal propagation, and distribution and structure of frontal turbulence and mixing, at a river plume front. The measurements are made using a novel platform that consists of a balloon-mounted infrared camera in combination with a vessel-mounted conductivity-temperature sensor chain. The sampling vessel was deliberately trapped in the convergent front, and followed it seaward for almost three hours during the ebb tide, so that the measurements were fixed in the frame of reference following the front. In this mode, the infrared images have been processed to generate high-resolution frontal velocity and turbulence fields, and a control volume approach is used to estimate the frontal mixing. We identify an approximately 16 m band of elevated mixing near the front based on the decay of turbulent kinetic energy (TKE) and TKE dissipation rate ( $\epsilon$ ). This region of frontal mixing is marked on the water surface by upwelling streaks of relatively cool water that extend landward from the front. Lobes and clefts were observed along the front that are characteristic of gravity currents observed in laboratory experiments. Turbulence is organized within the circulation of the lobes and clefts, with dissipation rates in the lobes being an order of magnitude higher than in the surrounding frontal regions.

## 23.1 Introduction

River plume fronts are sharp discontinuities in water properties such as salinity and temperature at the boundary of the plume (Garvine, 1974). These fronts are often visible on the flow surface as changes in colour arising from plume turbidity, or as foam lines resulting from convergence and downwelling at the front (O'Donnell *et al.*, 1998). Turbulence is elevated at the front relative to the plume interior (O'Donnell *et al.*, 2008; Kilcher and Nash, 2010) and mixing at the front has been estimated to

account for between 20% (Orton and Jay, 2005) to 100% (Pritchard and Huntley, 2002) of the total plume mixing. The dynamics of the plume front are typically modelled as buoyant gravity currents; Luketina and Imberger, 1987), citing the laboratory experiments of Britter and Simpson (1978). However, a large gap exists between the Reynolds numbers achieved in laboratory and numerical model gravity current experiments and the geophysical flows they are intended to simulate. Using new technology, high-resolution measurements of geophysical fronts, such as plume fronts, are now possible. This chapter presents

## 360 Coherent Flow Structures at Earth's Surface

observations of the buoyant gravity current generated by fresh, warm water discharged into the coastal ocean from the Merrimack River estuary, Massachusetts, United States. The frontal structure was observed from a front-following thermal infrared (IR) camera above the water surface and found to consist of a pattern of lobes and clefts. The IR measurements quantify the temporal evolution of a lateral structure within the plume front, which may have important implications for mixing and other frontal processes.

### 23.2 Background

In the experiments of Britter and Simpson (1978), a dense gravity current propagates across a free-slip boundary and develops a thick head region immediately behind the front, where intense mixing is initiated as Kelvin–Helmholtz instabilities. Similar experiments with a non-slip boundary also display another mode of instability, in which the front evolves a series of lobes and clefts with a wavelength 0.5 to 1.3 times the current thickness (Simpson, 1972; Simpson and Britter, 1979). The laboratory experiments of Britter and Simpson (1978) and Simpson and Britter (1979) both consisted of dense gravity currents that were arrested by an opposing current in the tank. The floor of the tank could be set at a variable speed conveyor belt so as to change the incident velocity profile or the bottom stress experienced by the gravity current. Experiments in a similar facility have been conducted since then at the University of Illinois (Garcia and Parsons, 1996; Parsons, 1998; Parsons and Garcia, 1998).

Britter and Simpson (1978) present a scale analysis that describes gravity current fronts in terms of the following scales:  $u_1$  and  $u_4$  are the frontal propagation speed and average speed of the water overtaking the front, respectively;  $H$  and  $h_4$  are the total flow depth and thickness of the layer of overtaking water, respectively;  $g'$  is the reduced gravity; and  $Q$  is the unit volumetric flow rate of buoyant or dense gravity current fluid introduced into the system. Dimensional analysis suggests that the arrested current can be described in terms of three dimensionless groups: the Froude number,  $Fr_H = \frac{u_1}{(g'H)}$ ; the height ratio,  $\frac{h_4}{H}$ ; and the mixing ratio,  $q = \frac{g'Q}{u_1^3}$ .

In the arrested front experiments,  $g'Q$  is the total buoyancy flux toward the head of the gravity current. Since the current is in a steady state, it must thus be equal to the flux of mixed fluid away from the front, and therefore represents the amount of mixing in the front.

Parsons and Garcia (1998) carried out experiments very similar to those of Britter and Simpson (1978), except that their facility was larger and thus extended to higher Reynolds numbers. Parsons and Garcia (1998) concluded that the mixing dynamics of the front are also sensitive to a fourth parameter, which they refer to as a buoyancy flux Reynolds number:

$$Re_Q = \frac{(g'Q)^{1/3}h_4}{\nu} \quad (23.1)$$

Although Britter and Simpson (1978) suggested that  $q$  is insensitive to Reynolds number and only a weak function of  $h_4H^{-1}$ , Parsons and Garcia (1998) observed that  $q$  is a strong function of  $Re_Q$  for  $Re_Q > 1000$ . Parsons and Garcia (1998) demonstrated that this transition accompanies a change in the mixing processes themselves, which was apparent in the scalar spectra and flow imaging.

More recently, Scotti (2008) carried out a series of direct numerical simulation (DNS) gravity current experiments in which changes were also observed in the mixing regime. However, the DNS runs are primarily at lower Reynolds numbers than the experiments of Parsons and Garcia (1998) and the transition was initiated by increasing the level of turbulence introduced into the ambient flow in front of the gravity current.

The formation of lobes and clefts has also been associated with an increase in mixing at the front (Simpson, 1982). Since lobes and clefts are typically assumed to occur only in gravity currents over a no-slip boundary, this implies that  $q$  would be higher in dense currents travelling over a fixed bed compared with buoyant currents travelling along a free surface.

Despite considerable effort over many decades to understand and parameterize the mixing rate at gravity current fronts, the vast majority of the research consists of laboratory and numerical model studies, which are limited to Reynolds numbers that are orders of magnitude smaller than those of the geophysical currents they intend to simulate. The principal objective of the current work is to provide a detailed description of the structure and mixing in the large-scale gravity current front at the edge of an ebbing river plume.

### 23.3 Field campaign and measurements

#### 23.3.1 Location and conditions

The Merrimack River discharges into the Atlantic Ocean on the border between Massachusetts and New Hampshire, United States. We observed the eastward-propagating plume front generated by discharge from

## 23 Coherent Structures and Mixing at a River Plume Front 361

the Merrimack River estuary during an ebb tide on 8 May 2010. Discharge during this period was approximately  $200 \text{ m}^3 \text{ s}^{-1}$ , which is similar to the Merrimack River annual mean discharge of  $214 \text{ m}^3 \text{ s}^{-1}$ . The observations were made during a neap tide when the tidal amplitude was approximately 2 m. The local wind was recorded with a roof-mounted anemometer located on the shore less than 1 km from the river mouth. During the ebb tide sampling, the winds were very low, and never exceeded  $4 \text{ ms}^{-1}$  during the main sampling period. Wind speeds were below the anemometer detection threshold of  $0.5 \text{ ms}^{-1}$  from 1:15 to 1:30 GMT, the focus period for the present analysis.

### 23.3.2 Measurements and sampling mode

We used an IR aerial remote sensing platform to detect the location of the front and to determine the frontal structure. The Lighter-than-Air-InfraRed System; (LTAIRS – Figure 23.1) consists of a lightweight computer and IR camera on a stabilized pan and tilt gimbal held aloft by a 3 m diameter helium balloon. The  $320 \times 240$  pixel IR camera is sensitive to temperature differences of 0.05 K, and at 50 m altitude the field of view was approximately 40 m by 30 m, resulting in a pixel resolution better than 0.1 m. Images were recorded to the balloon-mounted computer, which is controlled from on board the vessel via a wireless

display and keyboard. The system also records the GPS location of the balloon and camera tilt, pitch, and roll from an onboard inertial motion unit.

The IR images record the uncalibrated water temperature of the top  $10 \mu\text{m}$  of the water surface. These measurements are often subject to variations due to formation of a cool skin layer on the water surface that result from air-water heat flux (e.g. Saunders, 1967; Fairall *et al.*, 1996; Jessup *et al.*, this volume, Chapter 14). During the measurements reported here, however, the plume water was generally  $4^\circ\text{C}$  warmer than the coastal ocean and this contrast far exceeded differences due to the cool skin that are typically  $0.^\circ\text{C}$ . The surface IR field clearly delineates the plume frontal structure (Figure 23.2a), including upwelling of cool water immediately behind the front. In the IR images, lighter tones correspond to warmer plume water whereas darker tones correspond to cool ocean water.

In post-processing, the IR imagery was stabilized and rectified to the water surface. Horizontal velocity fields are generated from the rectified images using an IR particle image velocimetry (IR-PIV) technique developed by Chickadel *et al.* (2011; see also Jessup *et al.*, 2013). Validation of the IR-PIV by Chickadel *et al.* (2011) and Jessup *et al.* (2013) showed excellent agreement (within 2%) with a co-located *in situ* velocity measurement over an entire ebb tide in the Snohomish River estuary. The observed

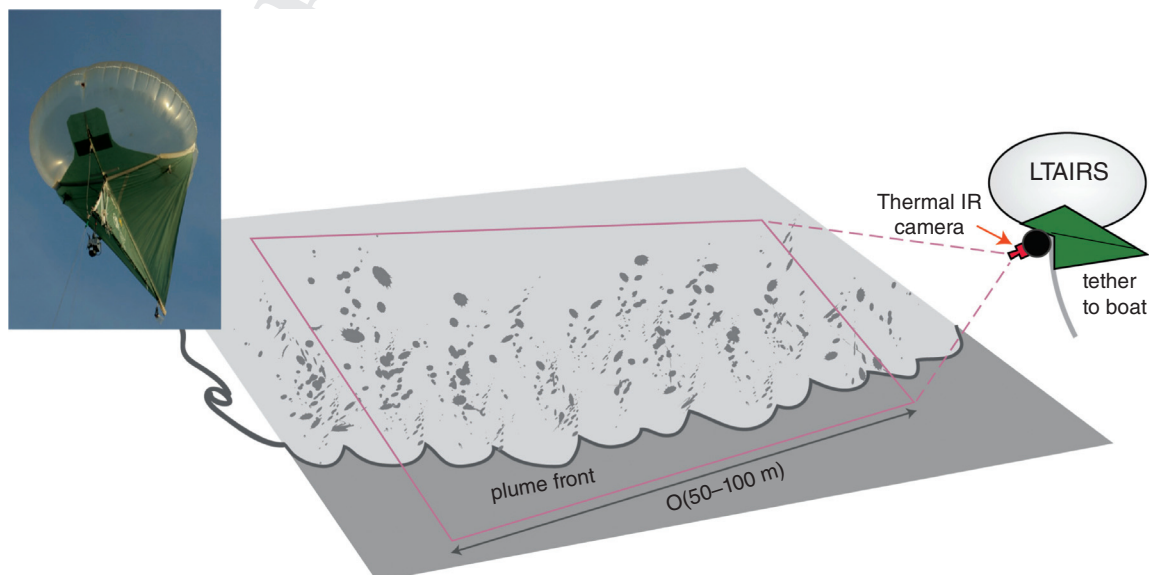


**Figure 23.1** The Lighter than Air InfraRed System (LTAIRS) sampling platform used to measure velocity structure in the frame of reference of the seaward-propagating river plume front.

## 362 Coherent Flow Structures at Earth's Surface

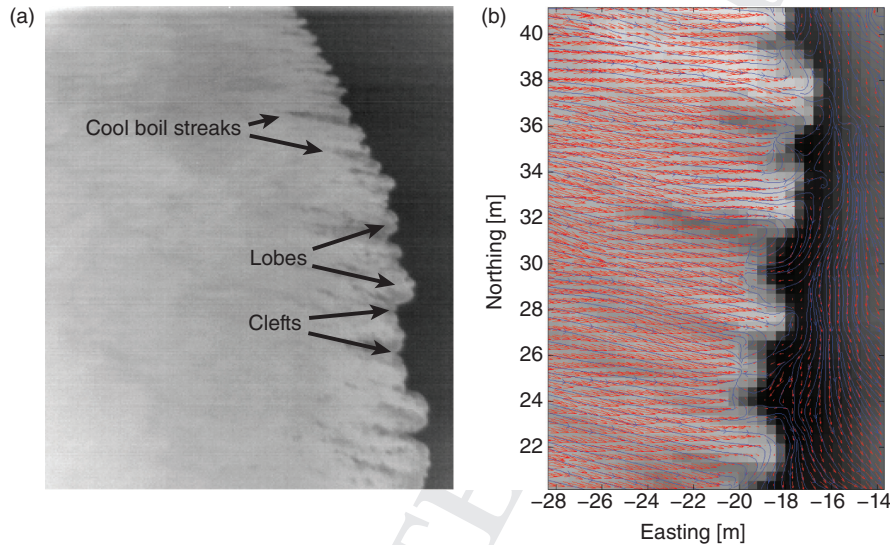


**Figure 23.2** (a) Infrared image of the Merrimack River plume front and (b) velocity field derived from the IR-PIV images. Light tones correspond to the plume water, which was approximately  $4^{\circ}\text{C}$  warmer than the ocean. Background flow in the ocean (dark, cooler water) is artificially flowing south due to the front-following mode of operation and image stabilization processing, and is in fact approximately zero velocity.

velocity (Figure 23.2b), which is in the frame of reference of the propagating plume front, indicates that the surface water in the region landward of the Merrimack plume front is overtaking the front with an average velocity of  $0.2\text{ ms}^{-1}$ .

A chain of six conductivity / temperature (CT) loggers, spaced evenly between the water surface and a point 2.5 m below the surface, was used to record the vertical density structure of the plume. The CT chain was suspended landward of the vessel as the front passed the boat in order to record the vertical structure at the nose and the frontal region of the plume. The plume was approximately 2 m thick and the temperature and salinity displayed a nearly identical vertical structure, with top-bottom differences of  $4^{\circ}\text{C}$  and 3 psu, respectively.

After crossing through the plume front for the first time, the vessel was subsequently carried seaward in the front due to surface flow convergence. The vessel was typically 10 – 15 m landward of the surface front when it was being carried seaward, presumably due to variation in the thickness and velocity structure of the plume near the front. In this mode, which was maintained for almost 3 h, measurements were made in a front-following frame of reference. The density measurements were immediately landward of the region of most intense frontal mixing, which is delineated in the IR images by the cool streaks extending landward from the front (shown by arrows in

Figure 23.2a). Finally, the vessel's GPS was used to track the seaward propagation of the front and determine the frontal propagation speed.

## 23.4 Results

### 23.4.1 Frontal propagation

The vessel initially intersected the front 0.7 km from the river mouth and subsequently followed it for more than 2 h, at which point it was 3.1 km from the mouth. The frontal propagation speed was calculated based on a linear fit to the frontal location  $x_f$  versus time data (Figure 23.3a) in 8 min bins and yielded an average value of  $U_f = 0.39\text{ ms}^{-1}$ . The reduced gravity of  $g' = 0.031\text{ ms}^{-2}$  and layer thickness of  $h = 2.0\text{ m}$  were determined based on the CT data. Based on these frontal values, the average frontal Froude number  $Fr = U_f (g'h)^{-1/2} = 1.56 \pm 0.24$ , which is slightly higher than the  $Fr$  of  $\sqrt{2}$  expected for freely propagating gravity currents (Shin *et al.*, 2004). The frontal Reynolds number based on the frontal speed and total depth  $H = 12\text{ m}$  is  $Re_f = U_f H \nu^{-1} = 4.8 \times 10^6$ .

### 23.4.2 Frontal structure and turbulence

The frontal structure observed in the IR images displays a clear lobe and cleft pattern (Figure 23.2a). Lobes protruding from the front have amplitudes and wavelengths of

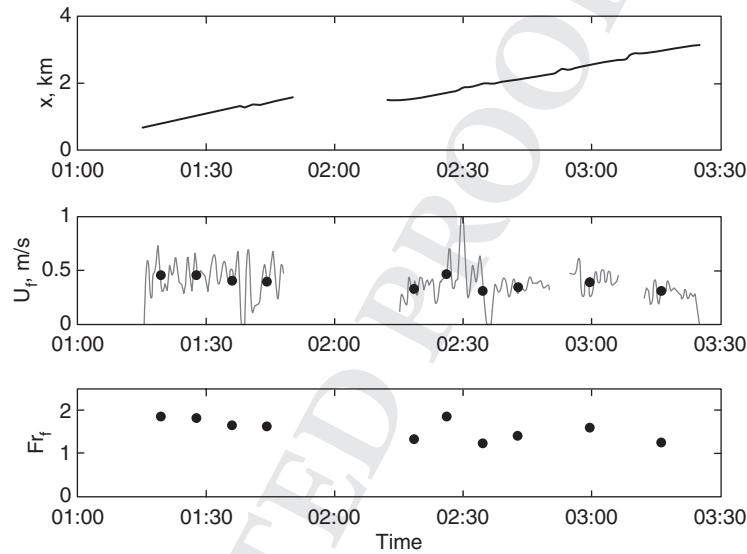


**Figure 23.3** (a) Frontal location taken from vessel GPS; (b) Frontal propagation speed based on the derivative of the data in (a) (line) and a linear fit to an 8-minute binned location – time date (dots), and (c) frontal Froude number.

approximately 1 m and 5 m, respectively, whilst the clefts are notches in the frontal edge that appear to be associated with cool boil streaks extending landward behind each cleft. These streaks are 5 – 15 m long and are presumed to delineate the region of most intense frontal mixing.

After image stabilization, the IR-PIV data provides a robust, stable measurement of the frontal velocity field. We compute a mean velocity field (Figure 23.2b), averaged over 20 s, and horizontal turbulent fluctuating velocities ( $u'$ ,  $v'$ ), by subtracting the mean field from instantaneous velocity fields. Based on the fluctuating velocities, the turbulent kinetic energy (TKE) and the TKE dissipation rate  $\varepsilon$  (Figure 23.4) were computed. The turbulent kinetic energy was defined using only the horizontal turbulent velocity components, assuming the vertical component is much smaller than the horizontal components at the water surface:  $TKE = u'^2 + v'^2$ . The dissipation rate is computed using the structure function methodology described by Wiles *et al.* (2006), who defined a structure function for the velocity co-variance  $D(x, r) = \overline{(v'(x) - v'(x+r))^2}$  as:

$$D(x, r) = C_v^2 \varepsilon^{2/3} r^{2/3} \quad (23.2)$$

where  $x$  is the spatial coordinate,  $r$  is the range and  $C_v^2 = 2.1$  is a constant. For a given point in the computed velocity field,  $D(x, r)$  is computed along a line parallel to the front and the fit to Eq. (23.2) is used to determine

$\varepsilon$ . The analysis of turbulence in the surface velocity field near the front (Figure 23.4) reveals elevated TKE and  $\varepsilon$  in the lobes and closer to the front (Figure 23.4). The TKE dissipation rate is approximately an order of magnitude higher in the lobes than it is in the clefts, indicating that turbulence is locally more intense there.

### 23.4.3 Frontal mixing

The front-following frame of reference affords a unique opportunity to measure mixing processes in the immediate vicinity of the plume front. These measurements are then used to determine the relative importance of frontal mixing in the total dilution of the plume, and can also be compared directly with laboratory estimates of frontal mixing to suggest the possible dependence of these results on the Reynolds number.

A control volume formulation is used herein based on that described by MacDonald and Geyer (2004) to estimate mixing. In this formulation, the difference between the advective flux of salt into one side of the control volume and out of the other side is attributed to vertical flux through the lower boundary of the control volume. Following MacDonald and Geyer (2004), the lower boundary is chosen as an isohaline surface, so that the flux through that boundary is actually a diahaline flux, rather than a purely vertical flux. This is more appropriate for understanding the rate at which salt is mixed into the plume front from the ambient ocean water. The formulation of

364 Coherent Flow Structures at Earth's Surface

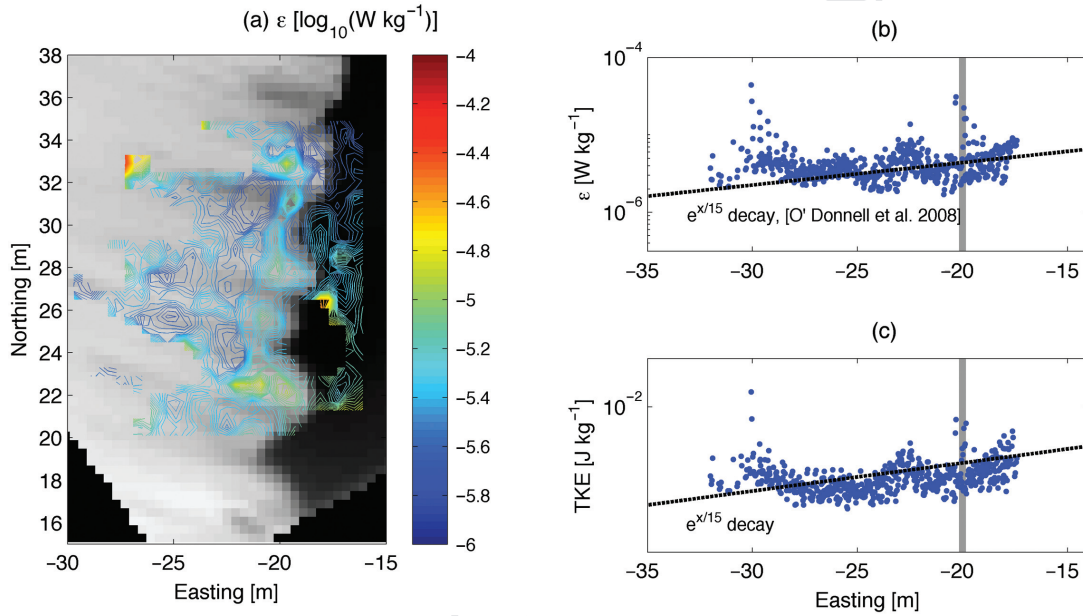


**Figure 23.4** (a) Spatial distribution of local estimates of TKE dissipation rate,  $\epsilon$ , near the plume front derived using the structure function approach applied to the surface velocity fields and overlaid on the average IR field. Cross-frontal decay of (b)  $\epsilon$  and (c) TKE. The dashed line shows the  $e^{x/15\text{m}}$  decay observed by O'Donnell *et al.* (2008) in a similar scale plume front. The vertical grey line shows the location of the plume front.

the control volume at the front (Figure 23.5) is different from that in MacDonald and Geyer (2004) and other similar implementations in two important ways. First, the control volume is moving with the frontal frame of reference; the front velocity is zero and the speed of the ambient ocean water beneath the plume layer is equal to the front speed (but in the opposite direction). Second, the control volume is a 'dead end' in that there is no flow out

of the seaward side. Instead, surface flow approaching the front is forced downwards, where it must cross isohalines before it is carried back out of the landward (left) side of the control volume.

The control volume salt balance is expressed as:

$$\frac{\partial}{\partial x} \int_{-h}^0 Sbu \, dz - \overline{Swb} = \frac{\partial}{\partial t} \int_{-h}^0 Sdz \quad (23.3)$$

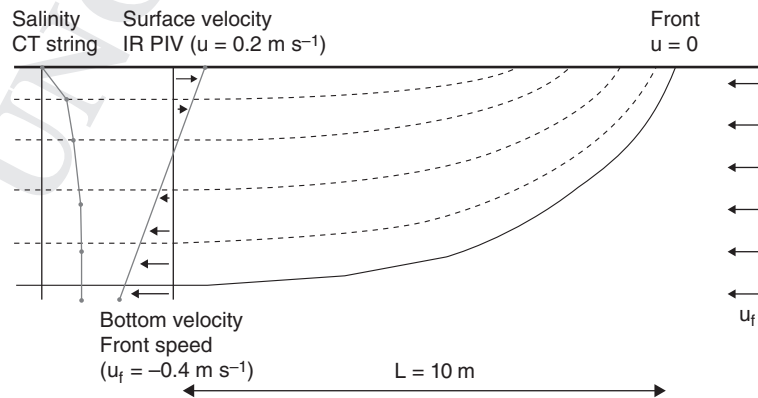


**Figure 23.5** Schematic diagram of the frontal control volume, showing the assumed isohaline surfaces (dashed lines) and location of the velocity and CT measurements used for the present analysis.

### 23 Coherent Structures and Mixing at a River Plume Front 365

where  $S$  and  $u$  are the salinity and velocity in the plume layer, respectively,  $b$  is the width of the control volume,  $h$  is the depth of the isohaline, and  $\overline{Sw}$  is the net diahaline salt flux through the bounding isohaline surfaces.

The control volume mixing analysis focuses on a 5 minute time period at 1:15 GMT when the data quality was highest, corresponding to the images presented in Figure 23.2b, and when the front was approximately 1 km from the river mouth (Figure 23.3a). As shown in Figure 23.2b, the approaching velocity 10 m landward of the front is relatively uniform and perpendicular to the front, and so it was assumed that the lateral fluxes were small and  $b$  is constant. The magnitude of the unsteady term on the right-hand side of Eq. (23.3) can be estimated based on the observed decay of the salinity anomaly over the sampling period (not shown). For the purpose of this estimate, it is assumed that the control volume consists of a 10 m long by 2 m deep triangle with a width  $b$ , and that it does not change in size significantly. The magnitude of the unsteady term per unit width is estimated as  $1.3 \times 10^{-3} \text{ m}^2 \text{ psus}^{-1}$ , which is more than an order of magnitude smaller than the first term on the left hand side of Equation (23.3). Assuming that the unsteady term is negligible, the net salt flux per unit width is equal to the divergence of the advective flux:

$$\overline{Sw} = \frac{\partial}{\partial x} \int_{-h}^0 S u dz \quad (23.4)$$

The implementation of this approach is also somewhat unique because of the available measurements. In the frontal frame of reference, we measured: (i) a six-point vertical CT profile approximately 10–30 m landward of the front, (ii) surface velocity relative to the front with the IR PIV, and (iii) the frontal propagation speed based on the vessel's GPS. In order to determine the advective salt flux through the landward boundary, it is necessary to estimate the shape of the velocity profile. We observe that the salinity profile is well approximated by a quadratic function of  $z$  (Figure 23.6a) and assume that the velocity will also be quadratic. This approximate shape is consistent with observations in the Merrimack River plume (MacDonald *et al.*, 2007). Thus,

$$S(z) = a_0 + a_1 z + a_2 z^2 \quad (23.5)$$

$$u(z) = b_0 + b_1 z + b_2 z^2, \quad (23.6)$$

where  $a_0$ ,  $a_1$  and  $a_2$  are constants determined from a fit to the salinity profile data (Figure 23.6a), and  $b_0$ ,  $b_1$  and  $b_2$  are constants to be determined. Two of the velocity constants can be determined from the known surface and bottom

velocities. To determine the third constant, we use the fact that the net freshwater flux through the profile must be zero,

$$\int_{-h_p}^0 \frac{S_0 - S(z)}{S_0} u(z) dz = 0 \quad (23.7)$$

where  $h_p$  is the plume thickness, which is assumed to be above the lowermost CT sensor, and  $S_0$  is the ambient salinity, taken to be the salinity at the lowermost sensor. This was verified by confirming that the salinity seaward of the front is approximately equal to the salinity at the lowermost CT sensor. Equation (23.5) is solved analytically for the final constant, but the polynomial solution is not reproduced here because it is long and cumbersome.

The resulting velocity and freshwater flux is directed toward the front near the surface and away from the front in the lower portion of the plume (Figure 23.6b and c). Note that the derived velocity profile does not have a zero gradient at the water surface, as would be expected for a zero-stress boundary. Since the stress was very close to zero, a zero-stress boundary condition could have been employed instead of the freshwater flux condition. However, the freshwater flux condition was determined to be more important for getting the mixing and salt balance correct within the front. MacDonald *et al.* (2007) also observed near-surface velocity profiles with shear all the way to the water surface, which suggests that the zero gradient region is very small. With these derived velocity and density profiles, the gradient Richardson number,  $Ri_g = \frac{g \frac{\partial \rho}{\partial z}}{\rho_0 (\frac{\partial u}{\partial z})^2}$ , could be estimated and yielded a value of  $Ri_g = 0.13$  when averaged over the full profile.

The net salt flux,  $\overline{Sw}$ , is determined from Eq. (23.4) using the quadratic salinity and velocity profiles, and is decomposed into mean and turbulent components according to:

$$\overline{Sw} = \overline{S} \overline{w} + \overline{S'w'} \quad (23.8)$$

where  $\overline{S}$ ,  $S'$ ,  $\overline{w}$ , and  $w'$  are the mean and fluctuating parts of the salinity and diahaline velocity, respectively. The velocity  $\overline{w}$  can be thought of as the entrainment across an isohaline with a salinity  $\overline{S}$ . The turbulent buoyancy flux is defined as

$$B = g \beta \overline{S'w'} \quad (23.9)$$

assuming all of the density variation is due to salinity, and where  $\beta = 7.7 \times 10^{-4} \text{ psu}^{-1}$ . In the present case, the temperature variation is non-negligible and is included in the final estimates of buoyancy flux. It is necessary to determine  $\overline{w}$  in order to solve Equation (23.8) for  $S'w'$

366 Coherent Flow Structures at Earth's Surface

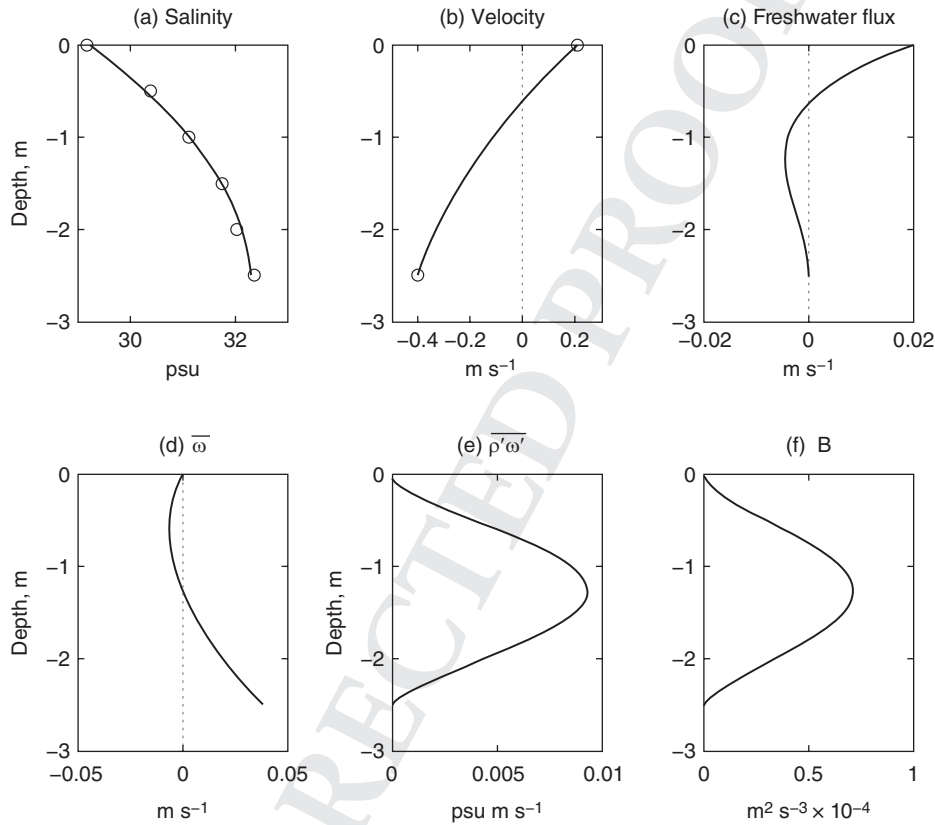


**Figure 23.6** Control volume results for: (a) salinity data (circles) and fit (line) averaged over 2 min, 15 m landward of the front. (b) Velocity profile derived from the control volume (line) using the measured surface and bottom velocities (circles). (c) Freshwater flux, (d) entrainment velocity, (e) turbulent density flux and (f) turbulent buoyancy flux derived from the control volume analysis.

and estimate the buoyancy flux. This is accomplished by solving the conservation of volume equation:

$$\bar{w} = \frac{\partial}{\partial x} \int_{-h}^0 u dz \quad (23.10)$$

For this calculation,  $h$  is taken to be the depth of a given bounding isohaline and the corresponding  $\bar{w}$  calculated from Eq. (23.10) is the entrainment through that isohaline. The values of  $\bar{w}$  for each salinity value between the plume base and the water surface were then plotted in terms of the corresponding depth (Figure 23.6d). The entrainment is found to be largest and positive at the base of the plume, indicating that water is being entrained upward into the plume layer. Within the top 1 m,  $\bar{w}$  is negative, indicating that plume water is being entrained downward toward the interface.

Finally, the turbulent salt flux,  $\overline{S'w'}$ , and the buoyancy flux  $B$  are calculated from Eq. (23.8) and (23.9) (Fig-

ure 23.6e and f). Both are zero at the bottom, where the salinity gradient approaches zero, and at the surface, where no diahaline flux is possible. The maximum buoyancy flux of  $0.7 \times 10^{-4} \text{ m}^2 \text{ s}^{-3}$  occurs half way through the plume, 1.25 m below the water surface. The mean buoyancy flux is  $0.4 \times 10^{-4} \text{ m}^2 \text{ s}^{-3}$ .

With these profiles, we can determine the scales used by Britter and Simpson (1978) to describe gravity current fronts in the laboratory. For the time period examined, the average velocity and thickness of the flow overtaking the front were  $u_4 = 0.1 \text{ ms}^{-1}$  and  $h_4 = 0.6 \text{ m}$ , respectively, and the frontal propagation speed and flow depth were  $u_1 = 0.4 \text{ ms}^{-1}$  and  $H = 12 \text{ m}$ , respectively. In the laboratory and DNS experiments, the buoyancy flux of the current,  $g'Q$ , is prescribed based on the volumetric input of dense fluid to the tank (in the case of negatively buoyant currents). The equivalent buoyancy flux approaching the plume front is not known *a priori*. The buoyancy flux

was determined by integrating the density and velocity profiles derived from the control volume analysis over the region of the profile approaching the front:

$$g'Q = g \int_{-h_4}^0 \frac{\Delta\rho}{\rho} u dz \quad (23.11)$$

and yielded a value of  $0.0015 \text{ m}^3 \text{ s}^3$ . The mixing ratio and buoyancy flux Reynolds numbers are therefore  $q = g'Q u_1^{-3} = 0.02$  and  $Re_Q = 6.9 \times 10^4$ , respectively.

### 23.5 Comparison to prior field and laboratory results

Britter and Simpson (1978) concluded that the frontal Froude number,  $Fr_4 = u_1 (g'h_4)^{-1/2}$ , is a function of the mixing ratio and the height ratio,  $h_4 H^{-1}$ . Measured values of  $Fr_4$  and  $h_4 H^{-1}$  from Britter and Simpson (1978), Luketina and Imberger (1987), Parsons (1998) and Scotti (2008) are shown in Figure 23.7. Relative to the data from these previous studies, the values obtained from the Merrimack front suggest that it is relatively thin, with  $h_4 H^{-1} = 0.05$ , and has a high Froude number  $Fr_4 = 2.7$ , consistent with expectations from the theory of Britter and Simpson (1978). The data point from the Merrimack is close to the observations from Luketina and Imberger (1987), which also corresponds to the front of a medium-sized river plume. Together, these data support the theory proposed by Britter and Simpson (1978) and further sug-

gest that buoyant plume fronts tend to occupy the high  $Fr_4$  range, due to their small height ratio.

The observed value of the mixing ratio is surprisingly low compared with previously documented values. Direct numerical simulation (DNS) (Scotti, 2008) and laboratory (Simpson and Britter, 1979; Parsons, 1998) studies typically report mixing ratios in the range from 0.1 to 0.4. The lack of imposed stress on the boundary cannot explain this difference because the results of Parsons (1998) include both slip and nonslip experiments. The observed mixing ratio is also an order of magnitude lower than the value of 0.15 estimated by Luketina and Imberger (1987) for a river plume front. It should be noted, however, that Luketina and Imberger (1987) were unable to directly estimate the buoyancy flux. Instead, they estimated the buoyancy flux based on the product of an estimate of the volumetric flux,  $Q$ , and a reduced gravity corresponding to the computed virtual origin of the circular frontal propagation. The buoyancy flux used to form the mixing ratio in the laboratory (Simpson and Britter, 1979; Parsons, 1998) and DNS (Scotti, 2008) experiments is based on the density anomaly and volumetric discharge of the flow introduced into the domain. Thus, both the laboratory experiments and the estimates from Luketina and Imberger (1987) form the mixing ratio based on the density anomaly well upstream of the front. An alternative estimate of the buoyancy flux for the Merrimack plume uses the reduced gravity of the inflow  $g' = 0.25 \text{ ms}^{-2}$ , which results in a mixing ratio of  $q = 0.24$ . This result is near the upper end of the range of previously reported

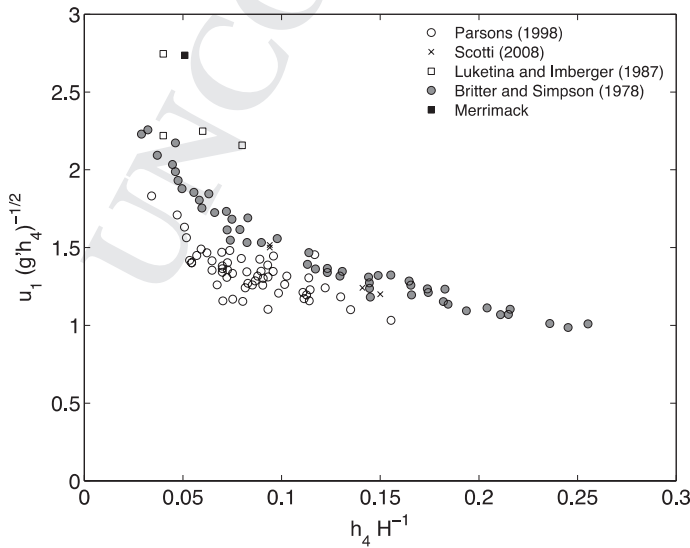


**Figure 23.7** Comparison of the Merrimack plume frontal Froude number with laboratory data from Britter and Simpson (1978) and Parsons (1998), DNS model data from Scotti (2008) and the Koombana Bay outflow front (Luketina and Imberger, 1987).

### 368 Coherent Flow Structures at Earth's Surface

results, suggesting that perhaps the buoyancy flux into the system, not the local buoyancy flux is the more appropriate scale.

O'Donnell *et al.* (2008) measured the turbulent kinetic energy dissipation rate in the Connecticut River plume front using a combination of ADCP, an automated underwater vehicle (AUV) equipped with shear probes, and a towed CTD. O'Donnell *et al.* (2008) report values of the gradient Richardson number from 0.04 to 0.15 close to the plume front, which bounds the present observation of 0.13. O'Donnell *et al.* (2008) also report estimates of the dissipation rate near the front ranging from  $1 \times 10^{-5}$  to  $6 \times 10^{-4} \text{ W kg}^{-1}$ . Within 20 m of the front measured in the present study, dissipation rates were around  $7 \times 10^{-6} \text{ W kg}^{-1}$  using the IR-PIV derived velocity fields, significantly lower than the estimates of O'Donnell *et al.* (2008). This difference is attributed to the damping of turbulence near the free surface; the order of magnitude differences between surface and subsurface dissipation estimates are consistent with damping due to the free surface observed in the Snohomish River estuary by the authors. It is also possible to estimate  $\varepsilon$  by assuming a flux Richardson number of 0.2 and computing  $\varepsilon$  based on the buoyancy flux determined using the control volume. This method gives a value of  $1 \times 10^{-4} \text{ W kg}^{-1}$ , within the range of the O'Donnell *et al.* (2008) estimates, larger than the value of  $1 \times 10^{-6} \text{ W kg}^{-1}$  reported by Luketina and Imberger (1989) for a smaller scale thermal plume, and lower than the maximum value of  $1 \times 10^{-3} \text{ W kg}^{-1}$  reported by Orton and Jay (2005) for the much larger Columbia River plume front.

These observations of frontal turbulence provide a measure of the width of the frontal region where mixing is most intense, which can be compared with the structure observed in the IR images. The intensity of turbulence near the plume front is observed to decay away from the front (Figure 23.4b and c), consistent with the predictions of Garvine (1974) that mixing decays exponentially behind the front. Exponential decay in the Connecticut River plume front was observed by O'Donnell *et al.* (2008), who estimated the decay scale to be  $L_G = 15 \text{ m}$  for that plume. The 15 m decay is shown on Figure 23.4b and c and is in reasonable agreement with our observations. In stratified shear flow experiments, Itsweire *et al.* (1993) found that buoyancy flux goes to zero approximately five buoyancy periods after its generation, and thus that the horizontal scale of mixing is as  $L_I = 5UN^{-1}$ . O'Donnell *et al.* (2008) show good agreement between this length scale and the decay of turbulence near the plume front. For the Merrimack River plume,  $L_I = 5u_1N^{-1} \cong 16 \text{ m}$ ,

which also agrees well with the decay of TKE and  $\varepsilon$  shown in Figure 23.4b and c. Finally, this scale is approximately equal to the length of the cool (darker) streaks observed in the IR images of the front (Figure 23.2). We therefore interpret the frontal region delineated by the cool streaks as the region of most intense mixing and suggest, following Itsweire *et al.* (1993), that buoyancy flux is largely shut down landward of this region.

The IR-derived turbulence measurements provide an unprecedented snapshot of the lateral structure of turbulence near the river plume front. This is, to the authors' knowledge, one of very few measurements of the lateral structure of turbulence in a geophysical-scale gravity current. We observe significant spatial variation in the intensity of the turbulence, with  $\varepsilon$  being an order of magnitude higher in the lobes than in the clefts. This elevated level of turbulence observed in the lobes is consistent with the DNS model results obtained by Cantero *et al.* (2007), who found that the Reynolds stress along the bottom of a dense, nonslip, gravity current was highest at the front and within the lobes. It is important to note, however, that the elevated turbulence observed in the plume front is not associated with bottom stress, as in the DNS results of Cantero *et al.* (2007), since the buoyant plume front travels along a free-slip water surface.

### 23.6 Summary

Using a novel front-following measurement platform, this paper has investigated the structure of turbulence and mixing in a river plume front, providing a rare opportunity to document the dynamics of gravity current fronts at a high Reynolds number. Although estimates of turbulent kinetic energy dissipation rate are consistent with other river plume-front estimates, the observed mixing ratio is an order of magnitude lower than that observed in laboratory and DNS studies. An alternative mixing ratio, which depends on the inflow density anomaly, is in better agreement with previous studies. The front is found to be organized into a pattern of lobes and clefts, and turbulence is observed to be significantly elevated within the lobes. Turbulence decays away from the front with a characteristic scale of 16 m, which is consistent with predictions from laboratory experiments on stratified turbulence. This decay scale is also consistent with the scale of the frontal mixing region delineated in the infrared images by cool streaks that extend landward from the front.

## References

- Britter, R.E. and Simpson, J.E. (1978) Experiments on the dynamics of a gravity current head. *Journal of Fluid Mechanics* **88**, 223–240.
- Cantero, M.I., Balachandar, S. and Garcia, M.H. (2007) High-resolution simulations of cylindrical density currents. *Journal of Fluid Mechanics* **590**, 437–469.
- Chickadel, C.C., Talke, S.A., Horner-Devine, A.R. and Jessup, A.T. (2011) Infrared-based measurements of velocity, turbulent kinetic energy, and dissipation at the water surface in a tidal river. *Geoscience and Remote Sensing Letters* **8**, 849–853.
- Fairall, C.W., Bradeley, E.F., Godfrey, J.S. et al. (1996) Cool-skin and warm-layer effects on sea surface temperature. *Journal of Geophysical Research* **101**, 1295–1308.
- Garcia, M.H. and Parsons, J.D. (1996) Mixing at the front of gravity currents. *Dynamics of Atmospheres and Oceans* **24**, 197–205.
- Garvine, R.W. (1974) Physical features of Connecticut River outflow during high discharge. *Journal of Geophysical Research* **79**, 831–846.
- Itsweire, E.C., Koseff, J.R., Briggs, D.A. and Ferziger, J.H. (1993) Turbulence in stratified shear flows: Implications for interpreting shear-induced mixing in the ocean. *Journal of Physical Oceanography* **23**, 1508–1522.
- Kilcher, L.F. and Nash, J.D. (2010) Structure and dynamics of the Columbia River tidal plume front. *Journal of Geophysical Research* **115**, C05S90. DOI: 10.1029/2009JC006066.
- Luketina, D.A. and Imberger, J. (1987) Characteristics of a surface buoyant jet. *Journal of Geophysical Research – Oceans* **92**, 5435–5447.
- Luketina, D.A. and Imberger, J. (1989) Turbulence and entrainment in a buoyant surface plume. *Journal of Geophysical Research* **94**, 12 619–12 636.
- MacDonald, D.G. and Geyer, W.R. (2004) Turbulent energy production and entrainment at a highly stratified estuarine front. *Journal of Geophysical Research* **109**, C05004. DOI: 10.1029/2003JC002094.
- MacDonald, D.G., Goodman, L. and Hetland, R.D. (2007) Turbulent dissipation in a near-field river plume: A comparison of control volume and microstructure observations with a numerical model. *Journal of Geophysical Research* **112**, C07026. DOI: 10.1029/2006JC004075.
- O'Donnell, J., Ackleson, S.G. and Levine, E.R. (2008) On the spatial scales of a river plume. *Journal of Geophysical Research* **113**, C04017. DOI: 10.1029/2007JC004440.
- O'Donnell, J., Marmorino, G.O. and Trump, C.L. (1998) Convergence and downwelling at a river plume front. *Journal of Physical Oceanography* **28**, 1481–1495.
- Orton, P.M. and Jay, D.A. (2005) Observations at the tidal plume front of a high-volume river outflow. *Geophysical Research Letters* **32**, L11605. DOI: 10.1029/2005GL022372.
- Parsons, J.D. (1998) Mixing Mechanisms in Density Intrusions. Ph.D. thesis, University of Illinois at Urbana-Champaign.
- Parsons, J.D. and Garcia, M.H. (1998) Similarity of gravity current fronts. *Physics of Fluids* **10**, 3209–3213.
- Pritchard, M. and Huntley, D.A. (2002) Instability and mixing in a small estuarine plume front. *Estuarine Coastal and Shelf Science* **55**, 275–285.
- Saunders, P.M. (1967) The temperature at the ocean-air interface. *Journal of the Atmospheric Sciences* **24**, 269–273.
- Scotti, A. (2008) A numerical study of the frontal region of gravity currents propagating on a free-slip boundary. *Theoretical and Computational Fluid Dynamics* **22**, 383–402.
- Shin, J.O., Dalziel, S.B. and Linden, P.F. (2004) Gravity currents produced by lock exchange. *Journal of Fluid Mechanics* **521**, 1–34.
- Simpson, J.E. (1972) Effects of the lower boundary on the head of a gravity current. *Journal of Fluid Mechanics* **53**, 759–768.
- Simpson, J.E. (1982) Gravity currents in the laboratory, atmosphere, and ocean. *Annual Review of Fluid Mechanics* **14**, 213–234.
- Simpson, J.E. and Britter, R.E. (1979) The dynamics of a gravity current advancing over a horizontal surface. *Journal of Fluid Mechanics* **94**, 687–703.
- Wiles, P.J., Rippeth, T.P., Simpson, J.H. and Hendricks, P.J. (2006) A novel technique for measuring the rate of turbulent dissipation in the marine environment. *Geophysical Research Letters* **33**, L21608. DOI: 10.1029/2006GL027050.

UNCORRECTED PROOFS